357

Submaximal exchange between a convectively forced basin and a large reservoir

By T. D. FINNIGAN and G. N. IVEY

Centre for Water Research, University of Western Australia, Nedlands,
Western Australia, Australia

If a sill-enclosed basin, connected to a large reservoir, is suddenly subjected to a de-stabilizing surface buoyancy flux, it will first mix vertically by turbulent convection before the resulting lateral buoyancy gradient generates a horizontal exchange flow across the sill. We present a study which examines the unsteady adjustment of such a basin under continued steady forcing. It is shown, through theoretical development and laboratory experimentation, that two consecutive unsteady regimes characterized by different dynamic balances are traversed as the flow approaches a steady state.

Once established the exchange flow is controlled at the sill crest where it is hydraulically critical. In the absence of a lateral contraction, the single control at the sill crest allows a range of submaximal exchange states with the flow at the sill being dependent not only on the forcing and geometrical parameters but also on mixing conditions within the basin which are, in turn, dependent on the sill exchange. The sill–basin system is therefore strongly coupled although it remains isolated from the external reservoir conditions by a region of internally supercritical flow. Results from the laboratory experiments are used to demonstrate the link between the forcing and the exchange flow at the sill. Steady-state measurements of the interior mean velocity and buoyancy fields are also compared with previous analytical models.

1. Introduction

The lateral exchange flow between two fluid bodies of different density is a classic fluid mechanics topic with many variations. One family of these flows involves a basin of limited horizontal extent which communicates with a large reservoir through some form of constriction. For an exchange flow to persist, the density gradient across the constriction must be sustained by either a source or a sink of buoyancy within the basin. In the latter case, there is a surface flow into the basin and a compensating deeper return flow (see figure 1). Geophysical examples of such systems include the Red and Mediterranean Seas, where the buoyancy sink occurs as an upward flux at the surface due to the combined effect of evaporation and cooling (Phillips 1966). Some Arctic fjords are subjected to similar forcing conditions when either cooled at the surface or when a growing layer of sea ice ejects brine and hence reduces buoyancy near the surface (Møller 1984).

The magnitude of the exchange flow q depends on the geometry of the constriction and on conditions in the adjoining water bodies. We confine our study to the case when a sill acts as the constriction and buoyancy is extracted uniformly from the surface of the basin. Starting with homogeneous density distributions in both basin and reservoir we investigate, through theoretical development and laboratory
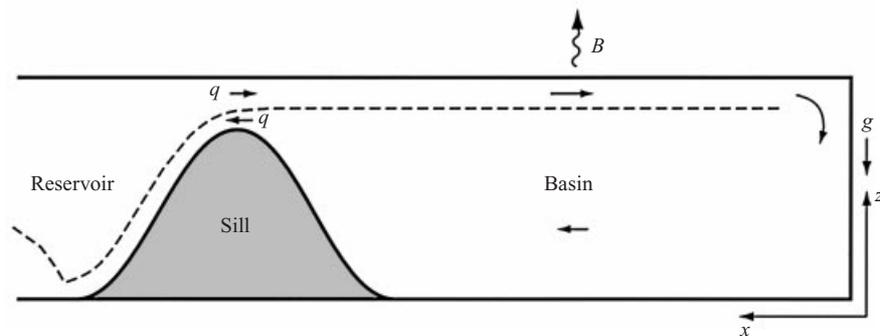
FIGURE 1. Sketch of the flow pattern for a sill-enclosed basin with buoyancy flux B at the surface. The exchange rate q at the sill depends on the buoyancy difference b between the counter-flowing layers, which is determined by conditions within the basin.

experiments, the unsteady response of the system when the surface buoyancy flux condition is suddenly applied and then held constant. The adjustment under these conditions is a model for what happens in natural systems that are exposed to rapid climatic changes, the onset of surface freezing, or large seasonal climate fluctuations.

With continued constant forcing the system will eventually reach a steady state with a surface current and deep return layer occupying most of the length of the basin. The buoyancy difference b between the layers at the open end of the basin reflects the extent of mixing between the layers within the basin. At the sill crest the flow is controlled, in a hydraulic sense, and b is thus directly related to q (e.g. Baines 1995). The sill and basin form a strongly coupled system with increased interior mixing having the effect of decreasing the buoyancy difference at the sill and increasing the exchange. If mixing is intense enough, a maximum exchange limit will be reached and further mixing beyond this point will not cause any further increase in exchange, leading to a situation where the basin is described as *overmixed* (Stommel & Farmer 1953). A *maximal exchange* state may also be achieved, without extensive mixing, when a second hydraulic control is present (possibly induced by a lateral channel contraction) and serves to isolate the exchange process from basin conditions (Farmer & Armi 1986). In §3 of the present paper we investigate the sill–basin relationship in the situation when a single control at the sill crest and moderate interior mixing result in *submaximal* exchange.

Previous authors have developed analytical models to predict the spatial variation of certain quantities, such as velocity and buoyancy, within the basin. Most of these studies have focused on the circulation within the Red Sea which has a similar configuration to the idealized system described in this paper. Phillips (1966) described the steady circulation within the Red Sea using a similarity formulation of the boundary layer equations. His model was extended by Tragou & Garret (1997) who assumed vertical turbulent diffusivity distributions and solved the equations to obtain the mean velocity and buoyancy fields. Their results matched field observations only when excessively large values of viscosity and diffusivity were used in the lower layer. As argued by Maxworthy (1997), these models neglected the influence of a hydraulic control at the sill near the open end of the sea and thus lacked an essential component of the strongly coupled sill–basin system. Maxworthy (1997) considered the connection between the hydraulic control at the constriction and the basin circulation, although he neglected the influence of interior mixing. Predictions from both of these models are compared with experimental results in §4 of the present paper.

In §2 we define the system of interest and describe the unsteady adjustment process which leads to a steady state. The relationship between the sill and basin flows is described in §3. Experimental methods and results are presented in §4 and conclusions appear in §5.

2. Description of flow regimes

2.1. *System description*

The idealized system of interest is shown in figure 1 where a rectangular basin on the right is separated by a sill from a large, essentially infinite reservoir. Initially the density distribution is everywhere homogeneous. The basin is suddenly subjected to an unstable surface buoyancy flux condition and this, in turn, initiates an unsteady response and gradual adjustment towards a steady state. The buoyancy flux is considered spatially uniform and steady once it has been initiated and we will generally refer to a thermally generated buoyancy flux since this is what was used for the experiments, although the discussion and results are equally applicable to other means of forcing (i.e. salinity).

Soon after the forcing is started thermals descend from the surface and turbulent convection ensues. The flow then proceeds through two different unsteady regimes before reaching the final steady state. To describe the processes involved in these flow regimes, we employ the unsteady equations of motion for two-dimensional inviscid turbulent flow, with the Boussinesq approximation. These may be expressed as

$$\frac{\partial u}{\partial t} + u\frac{\partial u}{\partial x} + w\frac{\partial u}{\partial z} = -\frac{1}{\rho_o}\frac{\partial P}{\partial x} - \frac{\partial \overline{u'u'}}{\partial x} - \frac{\partial \overline{u'w'}}{\partial z}, \tag{2.1}$$

$$\frac{\partial w}{\partial t} + u\frac{\partial w}{\partial x} + w\frac{\partial w}{\partial z} = -b - \frac{1}{\rho_o}\frac{\partial P}{\partial z} - \frac{\partial \overline{u'w'}}{\partial x} - \frac{\partial \overline{w'w'}}{\partial z}, \tag{2.2}$$

where u and w are mean horizontal and vertical velocities respectively, P is the mean pressure, primed quantities represent turbulent fluctuations about the mean and the overbar indicates a time average over a small duration with respect to variations in the mean quantities. The mean buoyancy,

$$b = \left(\frac{\rho_o - \rho}{\rho_o}\right)g, \tag{2.3}$$

is a result of the contrast between the mean local density, ρ, and that within the ambient or external reservoir, ρ_o, which is assumed constant. Evolution of the buoyancy field is governed by a transport equation,

$$\frac{\partial b}{\partial t} + u\frac{\partial b}{\partial x} + w\frac{\partial b}{\partial z} = \frac{\partial \overline{u'b'}}{\partial x} + \frac{\partial \overline{w'b'}}{\partial z}, \tag{2.4}$$

where $\overline{w'b'}$ represents the buoyancy flux due to turbulent vertical velocity fluctuations.

2.2. *Initial adjustment – Regime I*

A short time after the forcing is initiated the basin mixes over the entire depth by vertical turbulent convection. During this time, no buoyancy is exchanged across the sill. There is zero mean velocity within the basin and zero horizontal gradients due to the uniform surface forcing so equation (2.4) reduces to

$$\frac{\partial b}{\partial t} \approx \frac{\partial \overline{w'b'}}{\partial z}, \tag{2.5}$$
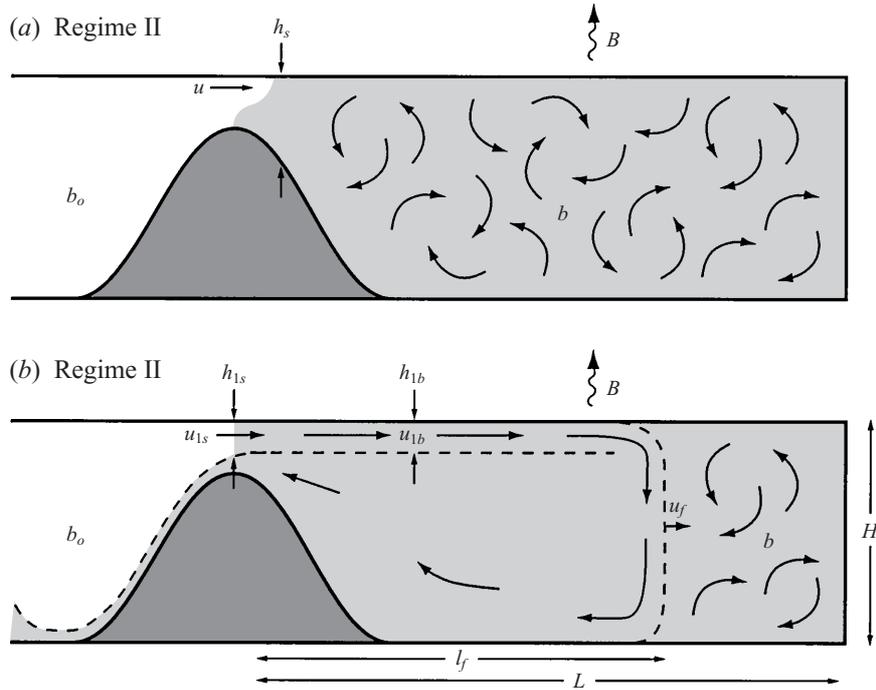
(a) Regime II

(b) Regime II

FIGURE 2. Depiction of flow during: (a) Regime I, and (b) Regime II.

which implies that the buoyancy field develops in response to vertical gradients of turbulent flux. At the surface the imposed buoyancy flux $B = \overline{w'b'}\big|_{z=0}$, while the magnitude of the interior buoyancy flux is expected to decrease towards the bottom (Adrian 1996) where it is obviously zero. By applying (2.5) at a location just inside the basin near the sill we obtain

$$b \sim \frac{Bt}{h_s},\qquad(2.6)$$

where h_s is the depth of the sill and the depth over which mixing must occur in order to decrease b. The situation described in this initial stage is depicted in figure 2(a) where the shaded region represents fluid with negative buoyancy. After combining equations (2.1) and (2.2) by cross-differentiating and then eliminating pressure terms, we observe that the magnitude of unsteady terms should approximately equal that of buoyancy terms or

$$\frac{\partial}{\partial z}\left(\frac{\partial u}{\partial t}\right) \sim \frac{\partial b}{\partial x},\qquad(2.7)$$

where we have assumed a predominantly horizontal response. The nonlinear inertia terms are expected to be relatively small since, at this stage, $u \approx w \approx 0$. In our experiments we have observed that the developing horizontal current is predominantly laminar at this stage (although it is driven by a buoyancy gradient resulting from turbulent convection in the interior) and the flux terms in (2.1) and (2.2) should therefore be relatively small. Inserting appropriate scales into (2.7) leads to

$$u \sim \frac{bh_s t}{l},\qquad(2.8)$$

where the length scale, l, represents the horizontal scale of the accelerating current. Combining (2.6) and (2.8) gives

$$u \sim \frac{Bt^2}{l}, \tag{2.9}$$

which is valid until convective inertia forces become comparable to the driving buoyancy forces or

$$\frac{\partial}{\partial z}\left(u\frac{\partial u}{\partial x}\right) \sim \frac{\partial b}{\partial x}, \tag{2.10}$$

which leads to

$$\frac{1}{h_s}\frac{u^2}{l} \sim \frac{b}{l} \sim \frac{Bt}{h_s l}, \tag{2.11}$$

and therefore

$$t \sim \frac{u^2}{B}. \tag{2.12}$$

If we assume that the velocity can still be approximated by (2.9) then (2.12) becomes

$$t_t \sim \frac{l^{2/3}}{B^{1/3}} \sim \frac{l}{(Bl)^{1/3}}, \tag{2.13}$$

where the subscript t has been added to refer to the time of *transition* from the scaling described above to the next regime which is described below. For the experiments described in §4 t_t is on the order of 30 s when l is taken to be the length of the current when it has extended beyond the sill region.

2.3. *Basin adjustment – Regime II*

After the initial adjustment in the sill crest region a lateral exchange is established and the flow moves into another unsteady regime depicted schematically in figure 2(*b*). For the first time, a layer of ambient fluid enters the basin and is progressively cooled as it flows a horizontal distance l_f under the forced surface and above a heavier counterflow. During this phase there still exists a region towards the end of the basin that is continually mixed by vertical convective processes, has no mean flow, and which is isolated from exchange with ambient or external fluid. The mean buoyancy in this region is given by

$$b \sim \frac{Bt}{H}, \tag{2.14}$$

which is similar to (2.6) except with h_s replaced by H (i.e. mixing over the full basin depth). The buoyancy in this end region is therefore continuously decreasing.

As shown in figure 2(*b*), the lateral surface current moves into the basin, loses buoyancy and then departs from the surface, descends and eventually flows back out of the basin. A vertical velocity front exists at a distance l_f from the leading edge of the forced surface. To avoid a lateral pressure discontinuity the surface current achieves a buoyancy deficit at the front which is equal to that in the end region. This also allows the neutral surface current to descend. The current flows back towards the open end of the basin without further significant change to its buoyancy as it is now remote from the forced surface. It is therefore the dynamics within the end region, and in particular the resulting value of b there, that determines the value of b in the outflowing layer and thus also affects the exchange rates at the sill where the flow is hydraulically controlled as explained below in §3. Since the buoyancy in the end region is continuously decreasing, the surface current must traverse progressively

further along the forced surface to accumulate a sufficient buoyancy deficit to match that in the end region and become locally neutrally buoyant at the front. As a result, the front slowly propagates along the length of the basin while *eroding* the end region.

Though time-dependence may not be negligible, we assume the dominant balance in the lateral surface current to be inertia–buoyancy. This amounts to a 'quasi-steady' or slowly varying assumption and from (2.1) and (2.2) we obtain

$$u_{1b} \sim (bh_{1b})^{1/2}, \tag{2.15}$$

where the subscript $1b$ refers to the upper layer within the basin (see figure 2*b*). The dominant stress terms in (2.1) and (2.2) may also be of the same magnitude as the terms retained in the derivation of (2.15) and a discussion of their influence is given in §3. Noting that the current loses buoyancy through the forced surface as it traverses a distance l_f, we may express the conservation of buoyancy as

$$Bl_f \sim u_{1b}h_{1b}b. \tag{2.16}$$

Combining (2.15) and (2.16) gives

$$u_{1b} \sim (Bl_f)^{1/3}, \tag{2.17}$$

and

$$b \sim \frac{(Bl_f)^{2/3}}{h_{1b}}, \tag{2.18}$$

which represents the buoyancy of the surface layer at l_f, and identically, the relative buoyancy between the layers at the sill crest. The relations (2.17) and (2.18) are analogous to the scaling results implied by Phillips' (1966) similarity formulation.

At l_f the buoyancy of the surface current equals that in the end region and we may therefore equate (2.14) and (2.18) which leads to

$$l_f(t) \sim B^{1/2}t^{3/2}\left(\frac{h_{1b}}{H}\right)^{3/2}, \tag{2.19}$$

thus determining the location of the front l_f at time t. The velocity of the front is given by

$$u_f = \frac{\mathrm{d}l_f}{\mathrm{d}t} \sim B^{1/2}t^{1/2}\left(\frac{h_{1b}}{H}\right)^{3/2}, \tag{2.20}$$

which indicates that the acceleration of the front decreases as it moves along the length of the basin. The surface layer velocity is found by combining (2.17) and (2.19),

$$u_{1b} \sim \left[Bt\left(\frac{h_{1b}}{H}\right)\right]^{1/2}, \tag{2.21}$$

and the ratio of u_f to u_{1b} is

$$\frac{u_f}{u_{1b}} \sim \frac{h_{1b}}{H}, \tag{2.22}$$

indicating that the front velocity is a fraction of the current velocity, depending only on the ratio of the surface layer thickness to the basin depth, H.

The scaling described above should be valid until the front reaches the endwall of the basin and $l_f = L$. The time of this occurrence is, from (2.19),

$$t_{ss} \sim L^{2/3}B^{-1/3}\left(\frac{H}{h_{1b}}\right), \tag{2.23}$$

which is also the time of transition into the steady-state regime, hence the subscript *ss*. For comparison, this time is of the order of 500 s for the experiments described below.

2.4. *Steady state – Regime III*

The flow reaches steady-state when the end region has been completely eroded and the front reaches the vicinity of the basin endwall. At this point b in the underflow is no longer determined by unsteady vertical convective mixing in the end region but is determined primarily by the buoyancy deficit acquired by the surface current as it traverses the basin length, L. The magnitude of b is given by (2.18) with l_f replaced by L,

$$b \sim \frac{(BL)^{2/3}}{h_{1b}},\tag{2.24}$$

and the corresponding relation for the horizontal velocity in the surface current is

$$u_{1b} \sim (BL)^{1/3}.\tag{2.25}$$

The above description is complicated by the fact that mixing between layers within the basin allows buoyancy values to differ from those which would occur in the absence of mixing. Mixing of deep fluid with relatively buoyant surface layer fluid has the effect of reducing the magnitude of b at the sill. This effect provides the dynamic link between sill and basin flows and we will show in §3 how it modifies the scaling laws described above.

2.5. *Summary of Regimes I, II and III*

The results of this section suggest that the flow passes through two different unsteady regimes as it proceeds toward the final steady-state regime. Scaling for the first regime is valid only for short times and it describes the initial adjustment at the sill and early acceleration of the exchange layers there. The second regime is characterized by a surface current which penetrates into the basin towards a front which propagates slowly towards the endwall, while the final regime has a surface current along the entire length of the basin. In the final regime, the surface flow continually loses buoyancy before reaching the endwall, plunging and returning over the sill.

Consider now the local horizontal velocity in the upper layer at the crest of the sill, u_{1s}. If we assume there is negligible vertical velocity nearby in the basin interior then conservation of mass suggests

$$u_{1s} = u_{1b}\frac{h_{1b}}{h_{1s}},\tag{2.26}$$

where u_{1b} is given by the scaling relationships developed in the above subsections and the subscript s refers specifically to flow variables at the sill crest. The sill velocity is expected to evolve as shown in figure 3 where curves for each of the three regimes are plotted with the intersections of the curves marking the transition points between regimes. A dark line traces the path of procession through the intersecting curves. Initially, the fluid accelerates rapidly according to the scaling for the first regime until it reaches a velocity equal to $\sim (l/L)^{1/3}$ of the steady state value at which time a front forms and the flow moves into the second regime. This occurs at time $t_t \sim (l/L)^{2/3}(h_{1b}/H)t_{ss}$ after which the flow follows the scaling of the second regime until $t \sim t_{ss}$ (equation (2.23)) upon which steady state is reached and $u_{1s} \sim (BL)^{1/3}(h_{1b}/h_{1s})$.
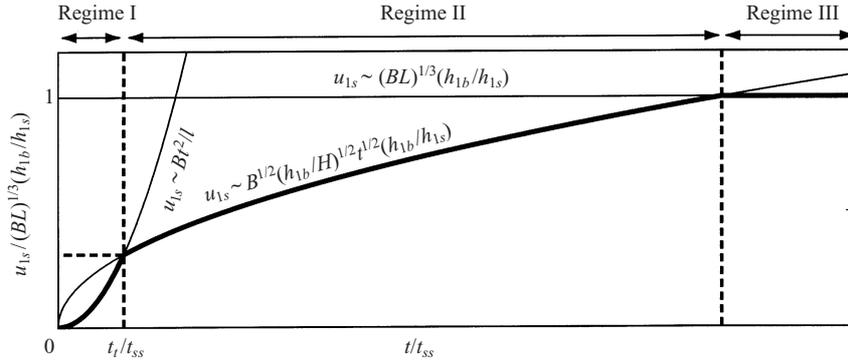
FIGURE 3. Theoretical representation of time variation of horizontal velocity at the sill crest. Thin lines represent the scaling laws derived in §2 and the thick line traces the procession of the horizontal velocity at the sill through the three flow regimes.

3. The sill–basin relationship

Two-layer hydraulic theory suggests that an internal hydraulic control can occur at the sill crest if the sill occupies a significant portion of the total fluid depth and if forcing is sufficient. At the control location the flow is termed *critical* and the composite Froude number $G^2 = 1$ (Armi 1986), where

$$G^2 = F_1^2 + F_2^2 - \epsilon F_1^2 F_2^2, \tag{3.1}$$

and

$$F_1^2 = \frac{u_1^2}{g'h_1}, \quad F_2^2 = \frac{u_2^2}{g'h_2} \tag{3.2}$$

are the densimetric Froude numbers for the upper and lower layers respectively, u_1 and u_2 are the mean horizontal velocities in each layer, $g' = ((\rho_2 - \rho_1)/\rho_2))g = \epsilon g$ is the reduced gravity with densities ρ_1 and ρ_2, and h_1, h_2 are the individual layer depths. It is assumed in the derivation of (3.1), and for hydraulic theory in general, that the flow is inviscid, has homogeneous density and velocity distributions in each layer, and a hydrostatic vertical pressure distribution. Where the fluid velocity is greater than the internal phase speed of long interfacial waves $G^2 > 1$ and the flow is termed supercritical. Similarly, the flow is subcritical and $G^2 < 1$ where the velocity is less than the phase speed.

The internal criticality at various locations is shown in figure 4. The sill control is essentially isolated from the reservoir since internal long waves are not able to propagate to the right through the supercritical region. The control, however, directly communicates with the subcritical basin, thus allowing an infinite number of possible submaximal exchange states determined by interior basin conditions (Farmer & Armi 1986).

Since the density difference between layers is small compared to the average density the composite Froude number may be written as

$$G^2 = F_1^2 + F_2^2. \tag{3.3}$$

At the sill crest $G^2 = 1$ and (3.3) specifies the relationship between the layer velocities u_{1s}, u_{2s} and thicknesses h_{1s}, h_{2s} for the local value of $g' = b$. In addition, mass conservation requires
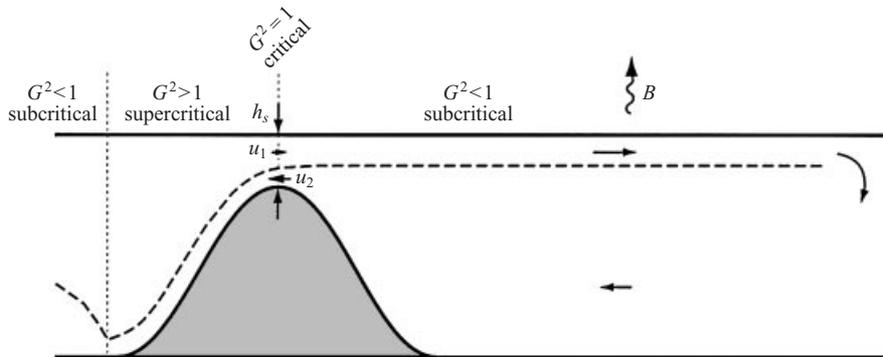
$$u_{1s}h_{1s} = u_{2s}h_{2s}. \tag{3.4}$$

FIGURE 4. Depiction of flow at steady state (Regime III). The flow is subcritical ($G^2 < 1$) everywhere within the basin, critical ($G^2 = 1$) at the sill crest, and supercritical ($G^2 > 1$) for some distance outside the basin. The composite Froude number, G^2, is defined in equations (3.1) and (3.2).

Combining (3.3) and (3.4) yields

$$\frac{u_{1s}^2}{b}\left(\frac{1}{h_{1s}} + \frac{h_{1s}^2}{h_{2s}^3}\right) = 1, \tag{3.5}$$

which applies at the sill crest. While this relation is valid (instantaneously) for the unsteady Regime II flow described in §2.3 we will focus on the steady Regime III flow.

The scaling results of §2.4 suggest that, since the entire flow is driven by the forcing in the basin, the resulting flow across the sill crest can be expressed as

$$u_{1s} = \beta(BL)^{1/3}\left(\frac{h_{1b}}{h_{1s}}\right) \tag{3.6}$$

and

$$b = \frac{\gamma(BL)^{2/3}}{h_{1b}}, \tag{3.7}$$

where β and γ are undetermined coefficients, dependent upon the turbulence field (and the associated mixing) within the basin as well as B, L and h_s. The coefficients β and γ allow us to include effects of comparable magnitude to those retained in the derivation of equations (2.24) and (2.25).

Since the flow parameters (u_{1s}, u_{2s}, h_{1s}, h_{2s} and b) are related by the criticality condition at the sill crest, the basin and sill flows must continually adjust towards an equilibrium state, which satisfies (3.5), (3.6) and (3.7). Combining these equations leads to

$$\frac{\beta^2}{\gamma} = \frac{h_{2s}^3}{h_{2s}^3 + h_{1s}^3}. \tag{3.8}$$

Noting that $h_s = h_{1s} + h_{2s}$ and inserting the buoyancy conservation condition, $BL = u_{1s}h_{1s}b$, we find the simple result that

$$\beta = \left(\frac{(h - h_{1s})^3}{(h - h_{1s})^3 + h_{1s}^3}\right)^{1/3} = \gamma^{-1}. \tag{3.9}$$

The coefficients in (3.6) and (3.7) are thus inversely proportional and are functions only of the interface level at the sill crest. This level is generally not known (although
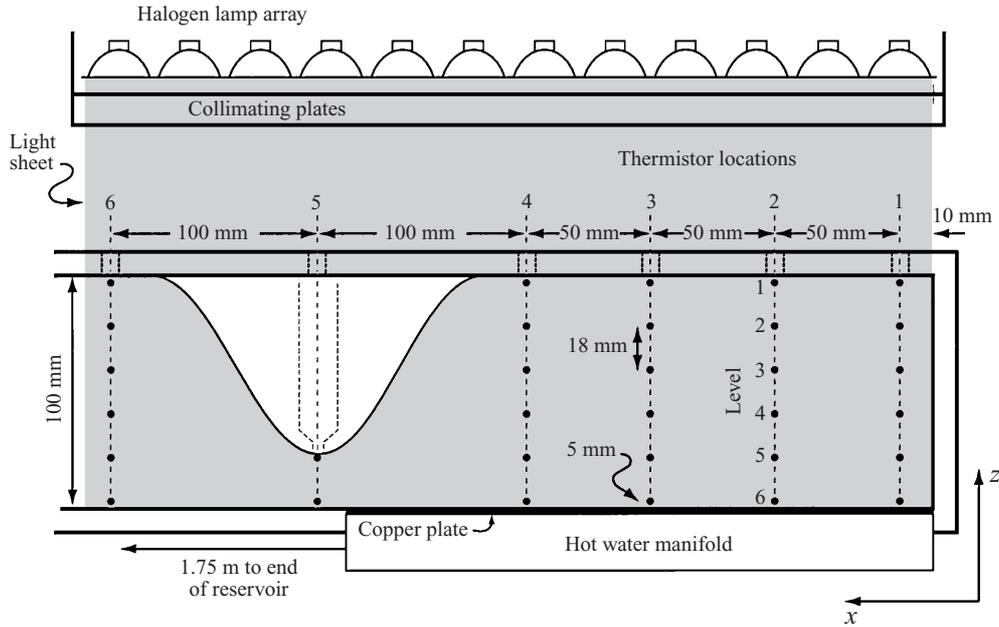
FIGURE 5. Configuration of experimental basin. The reservoir extends 1.75 m to the left of the basin. Thermistors were allowed to either traverse continuously along the dashed lines or stop at each dot (level) to record time series. The axis of the digital video camera was at 90° to the (x, z)-plane.

it may often be easy to measure) and is itself a result of the equilibrium state, which in turn depends on mixing within the basin. This implies that the interface position is an indicator of the total mixing in the basin.

4. Laboratory experiments

4.1. *Experimental methods*

The experiments were performed in an insulated rectangular tank with dimensions: $L_{tank} = 2000$ mm by $W = 500$ mm by $H = 100$ mm, and the forced basin occupied one end of the tank. The original laboratory facility is described by Sturman & Ivey (1998) who report on convectively driven exchange from a uniform basin without topographical influence. The tank was modified for the present experiments by adding a sill at the basin entrance which allows a minimum fluid depth of $h_s = 25$ mm and has a maximum width at its base of 150 mm. The sill crest was positioned 10 mm from the edge of the forced surface which extends $L = 250$ mm from the endwall of the tank. All experiments were actually performed 'up-side down', as shown in figure 5, with heating imposed at the lower surface, as this configuration allowed thermistors to interrogate the basin through ports in the un-obstructed upper boundary, opposite the forced surface. An experiment was begun by circulating heated fluid from an external constant-temperature bath through a manifold attached to the outer side of a copper plate representing the forced surface. Thermistors at the manifold inlet and outlet were used to detect the temperature change due to heat lost through the plate, ΔT, and together with the volume flow rate through the manifold, Q, the buoyancy flux (per unit area) through the plate could be computed as

$$B = g\alpha Q\Delta T, \tag{4.1}$$

Experiment	$T_{\text{manifold}} - T_{\text{ambient}}$ (°C)	$B \times 10^6$ (m² s⁻³)
1	10	1.2
2	17.5	6.5
3	25	9.2
4	4	0.6
5	32.5	17

TABLE 1. Surface buoyancy flux for each experiment.

where α is the thermal expansion coefficient for water at the mean manifold temperature.

Data for both temperature and velocity were acquired during the experiments over planes in (x, z) space. Thermistors traversed the depth of the basin while sampling the temperature at a rate of 100 Hz. Note that thermistor 5 actually traverses through a hollow region in the centre of the sill and emerges through a small hole at the crest before sampling across the depth h_s. Alternatively, the thermistor array was positioned at one of the six depth levels indicated in figure 5 and held there for 180 s while sampling continuously at 100 Hz. Assuming that the length scale of the largest eddies in the basin $l \sim H$ and the corresponding turbulent velocity scale $w' \sim (BH)^{1/3}$ (Deardorff 1970), then the largest turbulent time scale is

$$t_l \sim \frac{H}{(BH)^{1/3}} = \frac{H^{2/3}}{B^{1/3}}, \tag{4.2}$$

which is approximately 20 s for our experiments. Therefore a sampling duration of 180 s was chosen to provide statistical confidence over the full range of turbulent scales.

Two-dimensional velocity information was acquired using digital particle image velocimetry (DPIV) which utilizes statistical cross-correlation methods (Stevens & Coates 1994) to detect particle pattern displacements between sequential images. A high-resolution digital CCD camera was aligned with its viewing axis perpendicular to a light sheet and it was focused on the illuminated particles within either a 400 mm × 100 mm or a 270 mm × 100 mm field of view. The accuracy of the results depends on the characteristics of the flow and whether mean or fluctuating velocity values are being measured (Westerweel, Dabiri & Gharib 1997).

Since it is the buoyancy gradients that drive the convection and thus the entire system, the vertical orientation is irrelevant and we will present all further discussion and results in an intuitive geophysical sense (i.e. right-side up and referring to cooling at the top).

4.2. *Experimental program*

Listed in table 1 are five experiments which were performed at different values of the surface buoyancy flux, B. Experiments 1, 2 and 3 span the middle range of possible buoyancy flux values with our facility. After the start of each experiment velocity and mean temperature data were acquired through the unsteady adjustment period approximately every minute up to a time of 20 min, by which time steady state had been reached. While at steady state time series were recorded at each depth shown in figure 5 and velocity data were again acquired every minute.

Experiments 4 and 5 comprise the respective limits of the available buoyancy flux range. Experiment 4 was intended to reveal the behaviour with relatively low

turbulence intensity and weak stratification, while experiment 5 was intended to explore the opposite. For each of these two experiments, the emphasis of the data acquisition was on (i) fine temporal resolution of the unsteady velocity fields, (ii) resolution of the mean velocity field at steady state, and (iii) resolution of the mean buoyancy field in the surface layer at steady state. To achieve the first aim, velocity data were acquired at 10 s intervals following the start of an experiment. For experiment 4 this was continued for 400 s, and for experiment 5 for 700 s. To resolve the mean velocity fields at steady state, data were obtained from 50 image pairs for experiment 4 and from 70 image pairs for experiment 5, always at arbitrary time intervals of approximately 20 s between image pairs. These data were then averaged to remove the turbulent component and obtain the mean. The mean buoyancy field was obtained similarly from temperature time series recorded at thermistor level 6.

4.3. *Observed flow structure*

The structure of the flow for each regime is outlined in figure 6 which shows results from experiment 3. Figure 6(a) shows velocity (i) and buoyancy (ii) distributions shortly after the surface is subjected to an outward buoyancy flux between 0 and 250 mm. This represents Regime I, where the flow is characterized by vertical convection which penetrates to the bottom and then continues to mix the basin and reduce its mean buoyancy. The measured velocity field shows the penetration of the convection and the six buoyancy profiles indicate the negative buoyancy associated with the turbulent convected fluid. The vertical dashed line near each profile indicates the measurement location and also represents the reference buoyancy, $b_o = 0$.

Figure 6(b) shows the system at a later time when a lateral exchange flow has been established near the open end, an internal hydraulic control exists at the sill crest, and a region towards the closed end of the basin is still dominated by vertical convection with no mean flow (i.e. Regime II). A clearly defined, downward flowing and rightward propagating front is apparent at approximately 160 mm into the basin. A negatively buoyant supercritical stream may also be observed flowing down the outside of the sill before joining the reservoir fluid through a transition region. Note that the buoyancy within the basin has decreased further compared to the situation shown in figure 6(a ii), and that below the surface layer it is reasonably uniform as is to be expected since the downward flow at the front must have buoyancy equal to that in the end region (see §2.3).

In figure 6(c) the flow has reached steady state (Regime III) and an exchange flow now persists over the entire length of the basin. Again note that the buoyancy within the basin has decreased further to its final steady distribution. The surface flow is buoyant relative to the underflow, but the difference decreases as the flow traverses the basin, being cooled as it goes. Also note that the reservoir inflow at the sill crest has remained equal to the reference buoyancy b_o, while the outward-flowing lower layer has negative buoyancy. This layer exhibits a transitional structure on the left side of the sill which appears to evolve in form while the flow is unsteady.

The structure of the turbulence field at steady state is illustrated in figure 7 which shows buoyancy time series from experiment 3, obtained by converting measured temperature data to density and then calculating buoyancy from the definition in (2.3). The location where each time-series plot was measured is shown with reference to the basin. It is clear that the surface layer, flowing into the basin and sampled at thermistor level 6, is turbulent and decreases in buoyancy with distance into the basin. Large negative spikes in the signals at level 6 are the signatures of thermals descending through the surface layer. Near the end of the basin (location 1) the
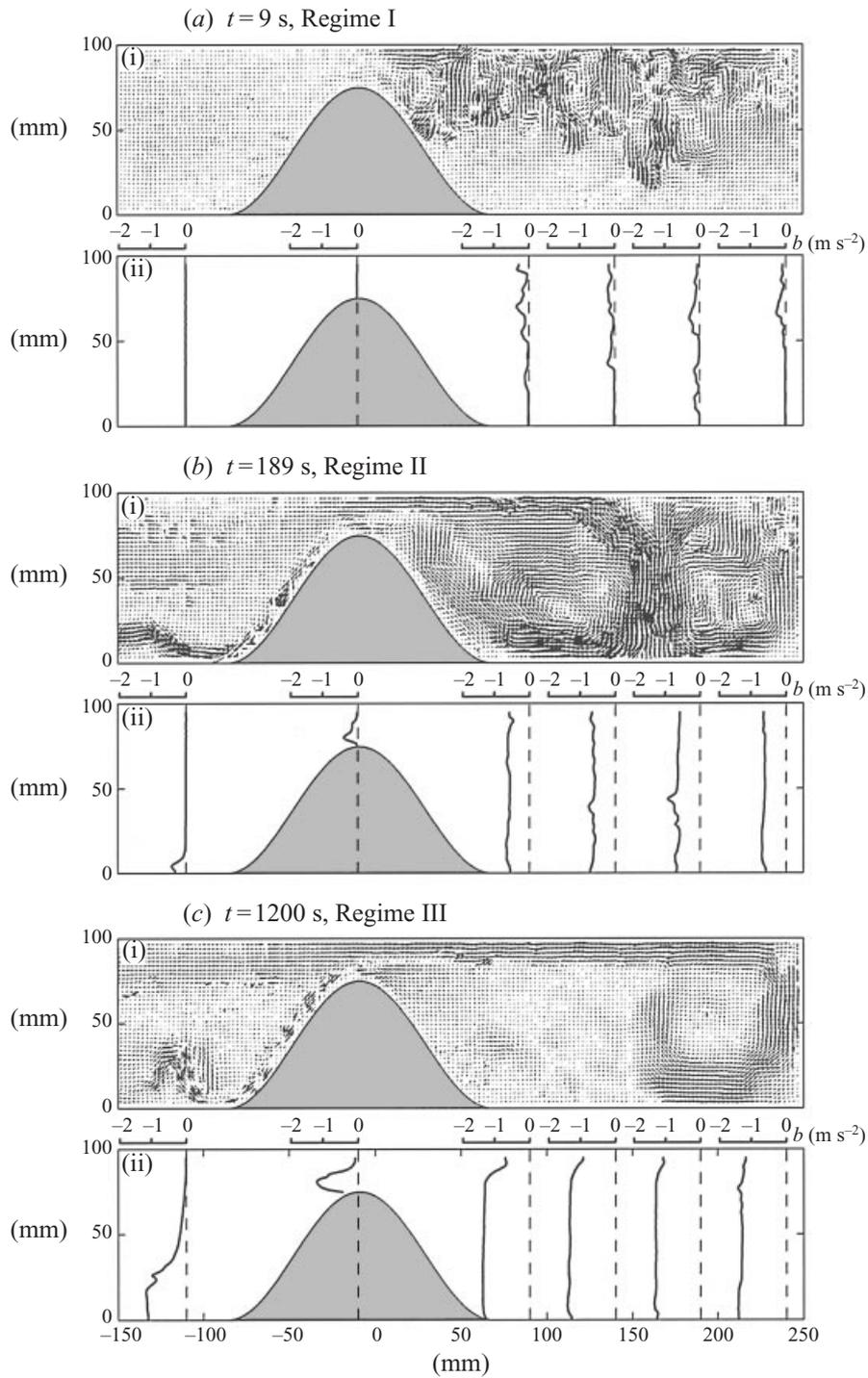
(*a*) $t = 9$ s, Regime I

(*b*) $t = 189$ s, Regime II

(*c*) $t = 1200$ s, Regime III

FIGURE 6. Observed velocity (i) and buoyancy (ii) field structures from experiment 3. Results represent flow during: (*a*) Regime I, (*b*) Regime II, and (*c*) Regime III. Note that buoyancy profiles only come to within 5 mm of the surface as indicated in figure 5.
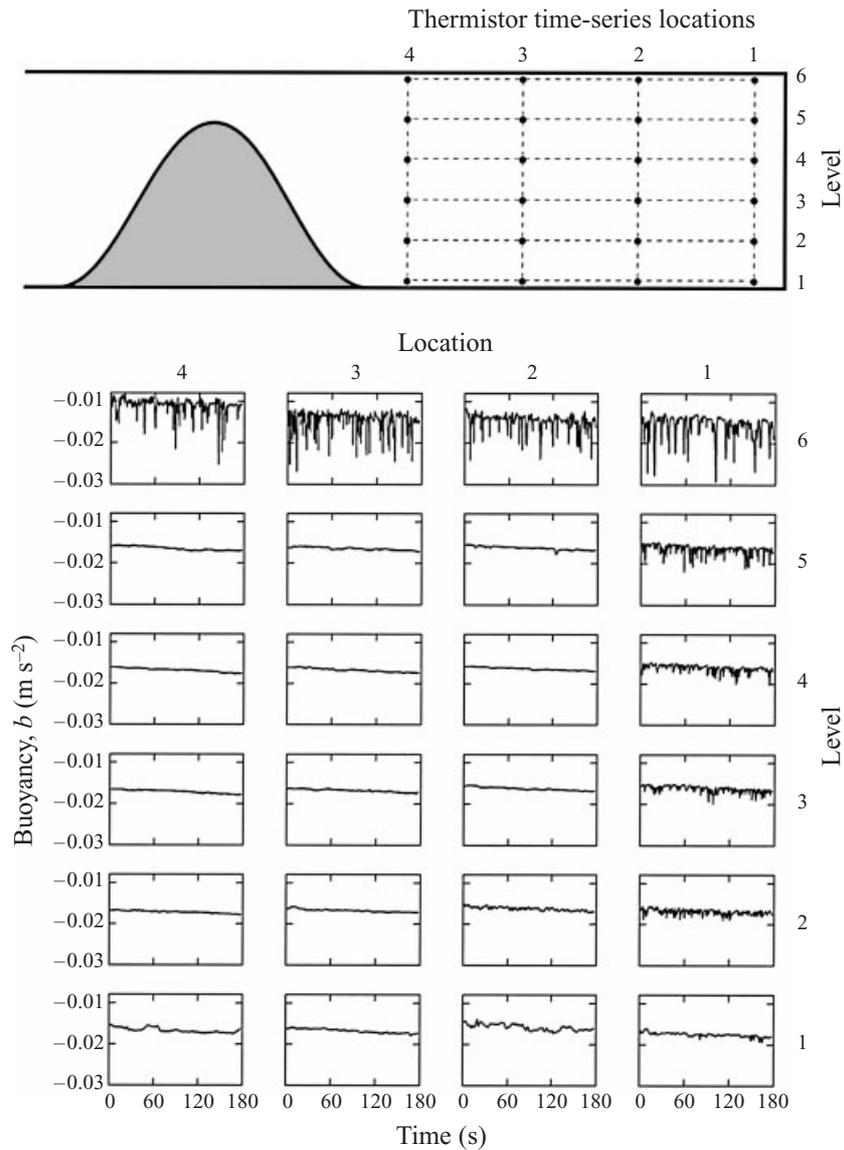
Thermistor time-series locations

FIGURE 7. Buoyancy time-series measurements for experiment 3. Each time series was recorded at a location indicated in the sketch of the basin. The ordering in the sketch is the same as the ordering of the plots.

turbulence is advected downwards and evidently decays rapidly once remote from the forcing surface. The return flow is predominantly laminar with a homogeneous buoyancy distribution.

4.4. *Initial adjustment – Regime I*

As described above, the initial period is characterized by convective mixing of the basin fluid and the acceleration, from rest, of the exchange layers at the sill crest. The scaling introduced in §2.2 should hold for the early part of this regime but becomes progressively inappropriate as the flow gradually moves into the second regime.
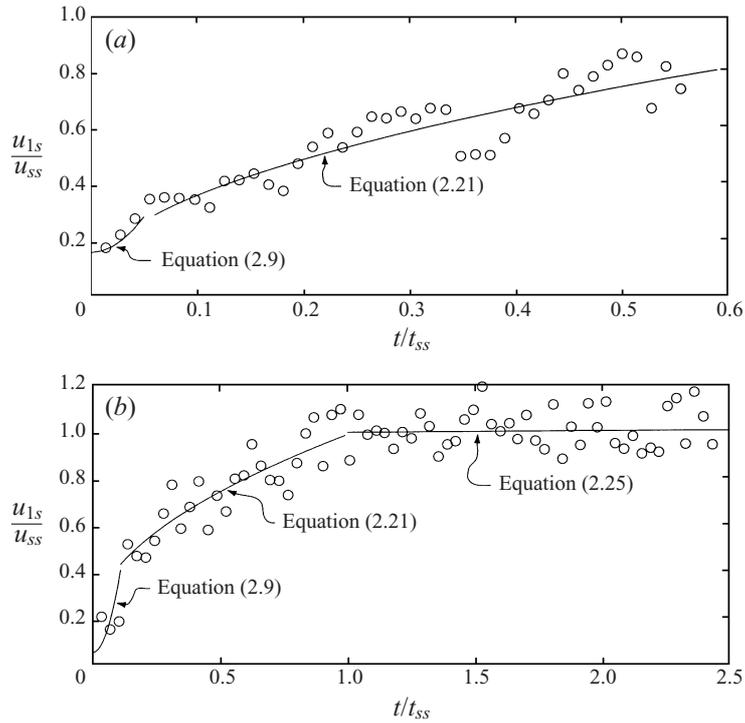
FIGURE 8. Observed variation with time of the horizontal velocity in the upper layer at the sill crest for (a) experiment 4 and, (b) experiment 5.

In figure 8 we have plotted the temporal variation of the upper-layer velocity at the sill crest (u_{1s}) for experiment 4 (panel *a*) and experiment 5 (panel *b*). Some oscillation about the mean is apparent in figure 8(*a*), indicating the presence of internal waves. This, as well as significant scatter, would tend to mask the expected behaviour in the early stages, making it difficult to assess the validity of (2.8).

4.5. *Basin adjustment – Regime II*

The scaling developed in §2.3 describes the time evolution of the surface velocity, $u_{1s} = u_{1b}(h_{1b}/h_{1s})$, the position of the front, l_f, and the buoyancy, b, in the end region, or identically, the buoyancy difference between the two counter-flowing layers at the sill crest (g').

Referring again to figure 8 we see that the scaling of (2.21) is in agreement with the observations for both experiments. Data for experiment 4 were only available up to approximately $t = 0.6 t_{ss}$ while data for experiment 5 extended beyond $t = t_{ss}$ where it is evident that the mean velocity assumes a constant value (equation (2.25)).

The oscillation about the mean velocity observed in figure 8(*a*) is likely to be due to internal waves propagating on the interface. The response is therefore a function of the effective horizontal scale of the interface, equal to l_f during this regime. Waves detected at the sill must all originate within the basin since none can propagate through the supercritical section outside the basin. We can estimate the wave speed, $c \approx (g'h)^{1/2}$, and therefore the period, $T \approx 2l_f/c$. Taking average values of $l_f = 15$ mm and $g' = 0.003$ m s^{-2} during Regime II of experiment 4, we obtain $T \approx 17$ s and $T/t_{ss} \approx 0.05$, which is of the same order as the dominant oscillation apparent in
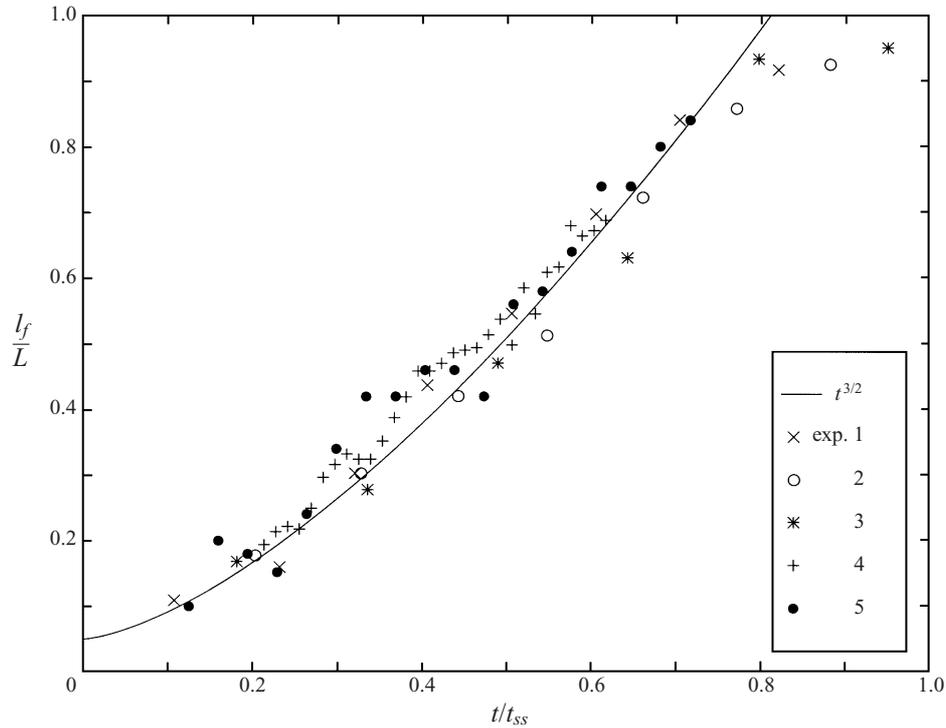
FIGURE 9. Propagation of the front during Regime II. The solid line represents equation (2.19) with a coefficient of 0.2 (i.e. $l_f(t) = 0.2B^{1/2}t^{3/2}(h_{1b}/H)^{3/2}$).

figure 8(*a*). Wave motions, however, are not within the focus of this paper and our primary focus below is on the mean velocity field.

As described in §2.3 a vertical front is expected to form and propagate along the basin. The observed front position along the basin is plotted in figure 9 as a function of time for all five experiments. The time axis is non-dimensionalized by the time for the front to reach the endwall or the time to steady state, t_{ss} (see equation (2.23)) and the vertical axis is non-dimensionalized by the length of the basin, L. A solid line, following the scaling for l_f given by (2.19), is plotted on the figure for comparison and it is clear that the proposed scaling is consistent with the observations for all five experiments. It is to be expected that as the front approaches the endwall the mixing in the end region may be affected by the presence of the solid boundary and the scaling may not apply, so close agreement near the top of the curve is not expected. The front motion is also likely to be influenced by large-scale turbulent overturning in the end region which may momentarily either enhance or retard the front depending on the orientation of the eddies. These effects probably account for the irregular trend observed in the data for experiment 5.

The ratio of the front velocity to the surface velocity was expressed in equation (2.22), which when combined with (2.26) gives the corresponding ratio at the sill, i.e.

$$\frac{u_f}{u_{1s}} \sim \frac{h_{1s}}{H}. \tag{4.3}$$

The velocity of the front is given by (2.20) with the appropriate coefficient (≈ 0.2) provided by the fit of (2.19) to the data shown in figure 9. The ratio in (4.3) was
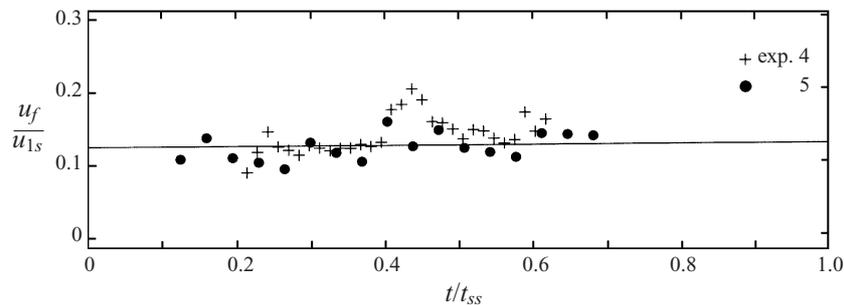
FIGURE 10. Time variation of the ratio of u_f to u_{1s} from results of experiments 4 and 5.

then formed using this result and values of u_{1s} from experiments 4 and 5. This ratio is plotted as a function of time in figure 10 where the wave signatures observed in figure 8 are again present. The ratio is approximately constant although there is a very slight increase, possibly due to the nonlinear relationship between u_{1s} and h_{1s}. If this is ignored then the implication of a constant ratio of 0.125 (solid line) is that $u_f/u_{1s} \approx 0.5(h_{1s}/H)$, but more experiments with other values of h_s are required to verify this.

4.6. *Sill–basin equilibrium (steady state) – Regime III*

As mentioned in §3 we can expect a single internal hydraulic control at the sill crest. This allows a range of submaximal exchange rates which depend on conditions within the basin. At steady state the flow has reached an equilibrium state determined through sill–basin co-adjustment. Unless there is substantial interior mixing, the equilibrium exchange rate at the sill will be submaximal. The equilibrium relationship between the coefficient β and the upper-layer thickness at the sill crest h_{1s}/h_s is shown in figure 11 where the solid curve represents equation (3.9). The portion of the curve below the maximal exchange point applies to the flows considered here. The upper portion does not appear to apply to any realistic situation since it pertains to layer thicknesses corresponding to a supercritical upper layer which would tend to isolate basin conditions from the control.

If the exchange is maximal the thickness of the surface layer at the sill crest $h_{1s} = 0.625h_s$ (Farmer & Armi 1986), and therefore $\beta = 0.562$ from (3.9). For sill-controlled submaximal flows $h_{1s} > 0.625h_s$ and $\beta < 0.562$. The coefficients, β and γ, are analogous to the similarity functions described by Phillips (1966) except in this case we are not speculating that these functions will exhibit similarity along the basin or be determinable below the surface layer, we are only looking at the values at the sill crest in the surface layer. The experimental results described in §4.7.1 below do indeed show that our flows are not necessarily similar.

Measured values of $\beta = u_{1s}/[(BL)^{1/3}(h_{1b}/h_{1s})]$ are plotted for all experiments at steady-state conditions in figure 11 along with the curve predicted by equation (3.9). The points fall consistently below the line, which could be due in part to viscous forces present in the experiments. As the buoyancy flux is increased, it appears that the flow moves away from the maximal flow state and the thickness of the upper layer increases. This type of response would continue with increasing forcing unless there was also an increase in mixing between layers within the basin. The end result would be a large value of b and a very thin, heavy lower layer which just trickles over the sill (e.g. Tragou & Garret 1997). Alternatively, the submaximal cases reported
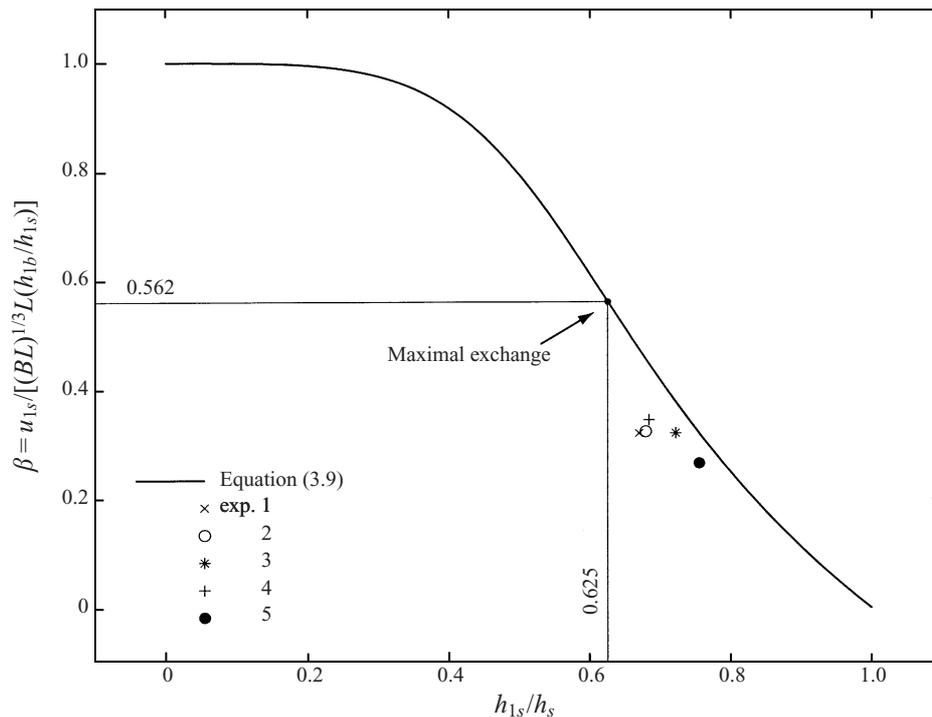
T. D. Finnigan and G. N. Ivey

FIGURE 11. The relationship between β and h_{1s} as predicted by the theory (solid line) and as measured for each experiment at steady state (symbols).

here could all be made to approach the maximal exchange limit if an independent agent for mixing in the basin were introduced. In fact, the distance between points for the most weakly forced case (experiment 4) and strongly forced case (experiment 5) seems small given the order of magnitude difference in surface buoyancy flux in the two cases. It is likely that some increase in mixing does accompany an increase in forcing and this retards the extent to which flows become submaximal (i.e. how far points move down the curve in figure 11). The smooth vertical variation of buoyancy, as observed in figure 6(*c* ii), indicates that mixing between layers does occur in the experiments, which is consistent with the observations at the sill (figure 11).

Values of $\gamma = \beta^{-1}$ derived from field measurements in the Red Sea were reported by both Phillips (1966) and Tragou & Garret (1997). In the context of their studies this parameter is referred to as the buoyancy function, g, and it is assumed in their analytical models to exhibit similarity along the basin, although Tragou & Garret (1997) showed that this is not always observed. Although the exact nature of the control (or lack thereof) in the Strait of Bab-el-Mandab is not well known, we may use their values of $\beta \approx 0.03$ (Phillips 1966) and $\beta \approx 0.015$ (Tragou & Garret 1997) to interpret the Red Sea flows assuming sill-controlled conditions. These two values are near the bottom of the curve in figure 11, indicating that the Red Sea exchange is submaximal and that mixing within the basin is only slight. For these values $h_{1s}/h_s \approx 0.05$ which means that the thickness of the dense outflow layer at the sill is approximately 1/20 of the total depth. Maillard & Soliman (1986) reported observations suggesting that this thickness can be as large as 1/4 of the total depth. The latter result suggests that $\beta \approx 0.33$ which is close to our measured experimental

results. It appears overall that the Red Sea exchange is submaximal although it is not certain to what degree it is.

Experiments aimed at simulating the flow in a sill-enclosed Arctic fjord have been conducted by Møller (1984). The data were not sufficient to allow a direct comparison with the theoretical curve shown in figure 11; however, it appears that the exchange flows were submaximal and an increase in the surface buoyancy flux increased the upper-layer thickness near the sill, which is consistent with our results.

4.7. *Interior basin conditions at steady state*

4.7.1. *Velocity variation along the basin*

Predictions of the analytical models of Phillips (1966) and Maxworthy (1997) can be compared to the observed along-basin variation of mean variables in our laboratory experiments. According to Phillips' (1966) results, the coefficients β and γ in equations (3.6) and (3.7) should be constant along the basin, near the surface. This proposal stems from the assumption that there is continual downflow along the basin and that the turbulence adjusts to maintain an inertia–buoyancy–viscous balance, as occurs in a classic turbulent boundary layer. In our terminology, Phillips' (1966) equations, applied near the surface, look similar to (3.6) and (3.7) except with L replaced by x and h_{1b} replaced by h,

$$u_{1b} = \beta(Bx)^{1/3}, \quad b = \gamma\frac{(Bx)^{2/3}}{h}, \tag{4.4}$$

where x is taken positive in the direction from the endwall towards the sill. Maxworthy (1997) has recently proposed an alternative to the above view which includes a two-layer system, with no mixing between layers but with shear-induced friction playing a dominant role. Equations resulting from this model are again similar to (3.6) and (3.7) except that the coefficients vary in x such that $\beta(x)$ eliminates the x dependence of u_{1b} and $\gamma(x)$ changes the buoyancy variation from $x^{2/3}$ to just x (i.e. linear variation). These results were also suggested earlier by Brocard & Harleman (1980), although the forms of the coefficients were slightly different.

In figure 12 we have plotted the variation of u_{1b}^3 with distance from the endwall for experiments 4 (panel *a*) and 5 (panel *b*). Each data point was obtained by averaging up to 70 individual turbulent velocity values resulting in a statistically representative mean. By Phillips' (1966) arguments we should expect to see the mean data follow a linear trend with positive slope. Phillips (1966) assumed that β is constant along the basin, in which case the slope of the predicted line is $\beta^3 B$, which is shown in figure 12 (solid line), for each experiment, and it is apparent that the surface current does not everywhere show the expected trend. Near the endwall ($x < 50$ mm) the flow is turning downwards and near the open end ($x > 200$ mm) the flow is accelerating into the basin over the sill and is not fully turbulent, so equations (4.4) are not expected to apply. In the basin interior, the trend for experiment 4 does generally follow the slope of the line but is complicated by both steeper and flatter regions while the trend for experiment 5 shows reasonable agreement between about 100 and 200 mm from the endwall. Maxworthy's (1997) model predicts that u_{1b} should remain constant along the basin and a horizontal dashed line representing this behaviour is also shown in figure 12. Over some portions of the basin this prediction is quite good, especially for experiment 5 between 50 and 170 mm from the endwall. This result suggests that β is a function of x and that the flows do not necessarily exhibit similarity over the entire basin.

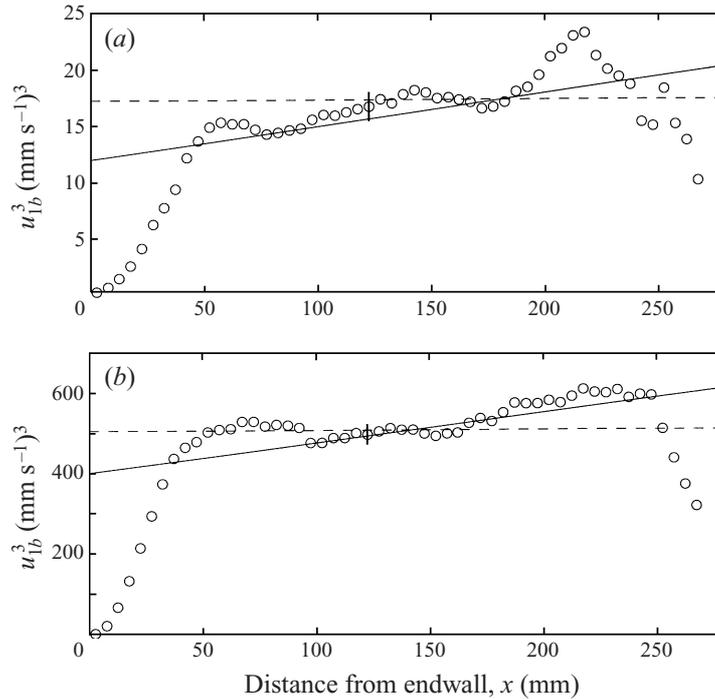The turbulent momentum and buoyancy flux fields are parameterized differently in

FIGURE 12. Mean surface velocity variation along the basin at steady state for (*a*) experiment 4 and (*b*) experiment 5, in comparison with the models of Phillips (1966) (solid line) and Maxworthy (1997) (dashed line). The vertical line near the centre of each graph represents $\pm$ one standard deviation of the measured mean values between $x = 50$ mm and $x = 200$ mm.

the two analytical models discussed here. A more extensive comparison of our results with the model predictions therefore requires detailed measurements of the turbulent momentum and buoyancy flux fields. This is beyond the scope of the present work but should be examined in future work.

4.7.2. *Buoyancy variation along the basin*

In a similar manner to that described above for velocity, we may investigate the horizontal variation of mean buoyancy within the basin. Figure 13 shows a plot of the mean buoyancy measured in the surface layer at steady state for experiments 1–5. The values were computed by determining the mean temperature over a 180 s time series and then converting the result to density before applying the definition in equation (2.3), where the buoyancy at each horizontal thermistor is referred to that in the ambient reservoir (location 6).

A line connects the points for each experiment and shows a near linear variation over most of the domain. This behaviour tends to support the prediction of the model by Maxworthy (1997). The $x^{2/3}$ dependence predicted by the Phillips (1966) model would appear as a decrease in the slope of the lines in the x-direction, and this is not apparent. Further experiments in a longer basin with finer sampling resolution and buoyancy flux measurements would be necessary to precisely determine the behaviour of the along-basin buoyancy distribution.
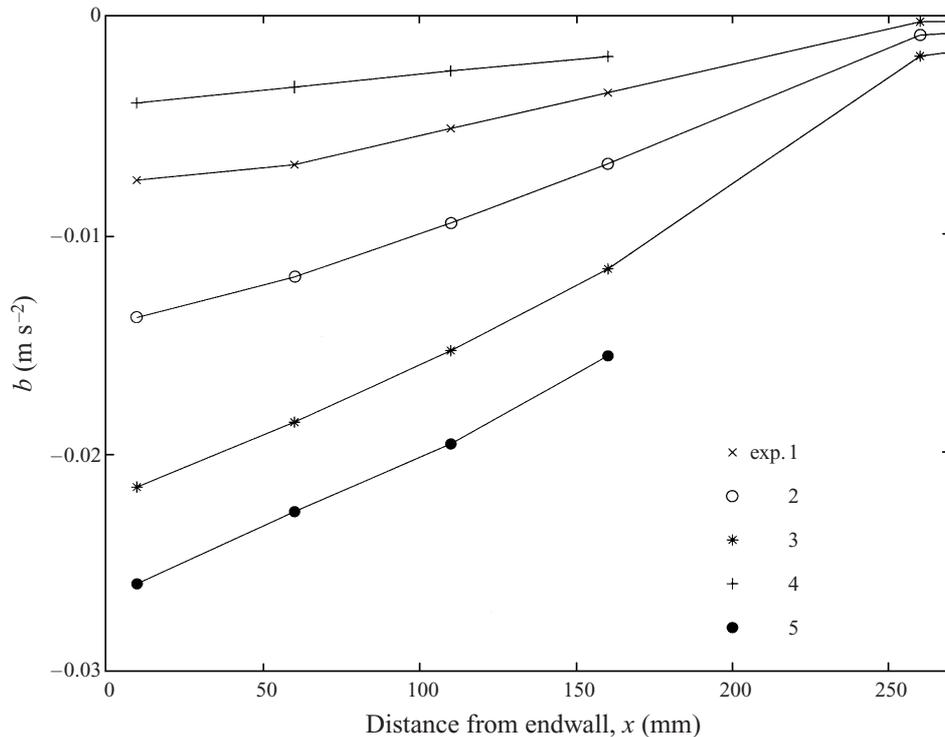
FIGURE 13. Mean surface buoyancy variation along the basin for experiments 1–5. Note that data at horizontal location 5 were not available for experiments 4 and 5 due to an instrument failure.

5. Conclusions

When a uniform and steady buoyancy flux condition is suddenly imposed at the surface of a sill-enclosed basin, such that the buoyancy of the surface fluid is reduced, an unsteady circulation ensues and the flow slowly adjusts towards a steady-state regime. We have outlined a progression of the flow through two distinct unsteady regimes as it adjusts towards a final steady state. The first immediately follows the onset of convection and it is characterized by turbulent mixing of the basin fluid, with zero mean velocity, and the acceleration from rest of two exchange layers at the sill crest driven by the local buoyancy-related horizontal pressure gradient. Once inertia forces become comparable to this pressure gradient a 'quasi-steady' surface current with steadily decreasing buoyancy is maintained by a balance between inertia and buoyancy. This current extends into the basin to a front before descending and returning to the sill where it is hydraulically controlled as it flows out of the basin. Continually decreasing buoyancy in a convectively mixed end region drives the propagation of the front and the slow acceleration of the surface current. Finally, a steady state is reached when the surface current occupies the entire length of the basin.

At steady state the velocity in the upper layer at the sill crest may be described by a scaling law ($u_{1s} \sim (BL)^{1/3}(h_{1b}/h_{1s})$) derived from an inertia–buoyancy balance. To obtain a more precise equation for this velocity the scaling result must be coupled with the hydraulic control which is in turn related to turbulence properties within the basin (see equation (3.6)). The turbulence, and any associated mixing, result in the value of the coefficient β which can be expressed as a function of the interface height